PACS: 61.05.C−; 61.10.Eq; 61.43.Gt; 61.46.+w; 68.37.Og; 68.43.-h; 68.47.Gh doi: 10.15407/hftp14.01.003

**V.M. Gun'ko, V.V. Turov**

# PARTICULATE MORPHOLOGY AND TEXTURAL CHARACTERISTICS OF NANOSILICA HYDRO-COMPACTED AT VARIOUS WETTING DEGREE

*Chuiko Institute of Surface Chemistry of National Academy of Sciences of Ukraine*
*17 General Naumov Str., Kyiv, 03164, Ukraine, E-mail: vlad_gunko@ukr.net*

*The particulate morphology and textural characteristics of nanosilica A–300, initial and hydro-compacted (cA–300) by wetting with various amounts of water in the range of h = 0.5–5.0 g per gram of dry silica, strongly stirred and then dried, have been analyzed using low-temperature $^1$H NMR spectroscopy (treated-dried-wetted samples), small angle X-ray scattering, scanning and transmission electron microscopies, infrared spectroscopy, and nitrogen adsorption methods (treated-dried-degassed samples). The effects of the hydro-compaction of A–300 depend strongly on the wetting degree with maximum changes at h = 1.5–2.0 g/g. The wetting degree could be varied to control the reorganization of aggregates of nonporous nanoparticles (NPNP, which are composed of tightly packed adherent proto-particles or nuclei) and agglomerates of aggregates (secondary and ternary structures, respectively), as well as visible particles; i.e., there is a penta-level structural hierarchy of nanosilica with three-level supra-NPNP structures. The hydro-compaction is accompanied by non-monotonic changes in the morphological and textural characteristics of cA–300 vs. h. However, the nanoparticles are much weaker affected by the treatment than higher hierarchical structures. At h ≤ 1 g/g, the reorganization of aggregate/agglomerate structures does not lead to diminution of the specific surface area (SSA); however, at h ≥ 1.5 g/g, the SSA value decreases, but the pore volume (estimated from nitrogen adsorption) increases despite the empty volume (estimated from the bulk density $\rho_b$) of the powder decreases from 21.8 cm$^3$/g for initial A–300 ($\rho_b$ = 0.045 g/cm$^3$) to 3.45 cm$^3$/g on hydro-compaction at h = 4.5 g/g ($\rho_b$ = 0.256 g/cm$^3$), pores become more ordered with a predominant contribution of cylindrical shapes. The textural reorganization of dried hydro-compacted nanosilica is possible again after addition of new water amount. This suggests that the chemical bonds between neighboring nanoparticles do not practically form upon the hydro-compaction and subsequent drying. Thus, hydro-compacted nanosilica loses a dust-forming property (since $\rho_b$ strongly increases), but it remains active with respect to the NPNP mobility, e.g., in aqueous media, and the possibility of the reorganization of the supra-NPNP structures remains under various external actions that is of importance from a practical point of view.*

***Keywords****: hydro-compacted nanosilica, wetted nanosilica, particulate morphology, textural characteristics, hierarchical structure reorganization*

## INTRODUCTION

Fumed nanosilica A–300 (studied here as a representative of nanosilicas and other fumed oxides) is composed of nonporous nanoparticles (NPNP of 5–20 nm in size, average diameter $d_{av}$ ≈ 10 nm, and composed of strongly adherent nuclei) forming aggregates (≤ 1 μm in size), agglomerates of aggregates (> 1 μm), and loose visible particles (supra-NPNP structures). Fumed silicas are synthesized using high-temperature (> 1000 °C) hydrolysis of silicon tetrachloride (or $SiCl_xR_{4-x}$ where R is organic functionalities) in a hydrogen/air flame that determine main characteristics and properties of the powder materials [1–13]. The powders of various nanosilicas have the specific surface area (SSA) $S_{BET}$ = 50–500 m$^2$/g and the bulk density $\rho_b$ ≈ 0.04–0.13 g/cm$^3$ increasing with decreasing $S_{BET}$. They are sensitive to any external actions such as wetting–drying, heating–cooling, adsorption, pressing, *etc.* due to weak bonds between neighboring NPNP of electrostatic, van-der-Waals, and hydrogen-bond origins in loose supra-NPNP hierarchical structures [14–24]. The intact fumed nanosilicas represent strongly dusting powders that can be considered rather as a negative property for various practical applications [1–15, 25–39]. Therefore, nanosilica compaction without a significant loss of its positive characteristics (high SSA value, NPNP activity, easy suspending and polymer filling, *etc.*) is of importance from a practical point of view. One of simple ways to modify nanosilica

characteristics without changes in the surface chemistry is hydro-compaction under standard conditions [17–20, 40–43]. High sensitivity of the nanosilica powders to wetting-stirring-drying-heating is due to multi-factor phenomena. Therefore, it is needed deeper insight into the problem to elucidate the dependences of the morphological, structural, and textural characteristics of the materials on the amounts of water used upon hydro-compaction treatment (or other treatments), as well as on other conditions. Note that porous silicas, such as silica gels, precipitated silicas, and others synthesized at relatively low temperatures in liquid media are characterized by more tightly binding of nanoparticles in rigid secondary structures (up to microparticles or macroparticles). After wetting-drying at room temperature (*i.e.*, without hydrothermal treatment) they do not practically change the particulate morphology and textural characteristics [14–18]. However, the hydro-compaction effects under standard conditions can be significant for nanosilicas with active, mobile NPNP that provides easy rearrangement of loose supra-NPNP structures quite characteristic not only for nanosilica but also for other fumed oxides [18–21, 40]. Therefore, the regularities analyzed here for nanosilica could be found for other fumed oxides [18–22].

Water as a polar and strongly structured liquid, in which all atoms in the molecules can form strong hydrogen bonds, tends to form clusters around silanols (or other polar or charged surface functionalities) at adsorbent surface. The water cluster sizes depend on the amounts of adsorbed water and adsorbent morphology and texture [14–22]. If the amount of water bound to a nanooxide is close to the volume of voids between NPNP (*e.g.*, estimated from nitrogen adsorption) that water can form a continue coverage of all nanoparticles that can affect the structural reorganization of the supra-NPNP structures [18–22, 44–48]. This important aspect is analyzed below for nanosilica as a representative of fumed nanooxides.

The aim of this work was to study the dependence of the characteristics of hydro-compacted nanosilica A–300 (cA–300) on the amounts of water used on wetting of the silica powder then mechanically treated (carefully stirred) and dried. Upon wetting–stirring–drying of nanosilica, there are additional important factors such as temperature and pressure. An increase in temperature and pressure (*e.g.*, upon hydrothermal treatment in steam or liquid phases) can result in very great changes in the particulate morphology and hierarchical structures of treated silicas [18, 40]. This is rather a negative result due to strong diminution of the SSA value, increase in particle sizes, dispersivity loss, *etc.* Therefore, in the present work, wetting-stirring of the nanosilica was carried out at room temperature to avoid strong reduction of the textural characteristics. Note that there are a set of factors differently affecting the studied phenomena [18, 40]. Therefore, several informative methods, such as small angle X–ray scattering (SAXS), nitrogen adsorption-desorption, infrared (IR) spectroscopy, scanning electron microscopy (SEM), high-resolution transmission electron microscopy (HRTEM), and low-temperature $^1$H NMR spectroscopy, have been used here to elucidate the influence the water content on the results of the hydro-compaction treatment of nanosilica in detail.

## MATERIALS AND METHODS

Fumed nanosilica A–300 (Pilot plant of Chuiko Institute of Surface Chemistry, Kalush, Ukraine; specific surface area $S_{BET}$ = 294 m$^2$/g and corrected $S_{BET}$ = 275 m$^2$/g [49] (*vide infra*), bulk density $\rho_b \approx 0.045$ g/cm$^3$) was used to prepare hydro-compacted (then dried) nanosilica (cA–300) powders (Table 1). Nanosilica A–300 is composed of nonporous nanoparticles (NPNP) of ~ 10 nm in average diameter. NPNP form aggregates (< 1 μm in size) and loose agglomerates of aggregates (> 1 μm in size) (Figs. 1 and 2) forming visible structures characterized by a low value of $\rho_b$. Initial nanosilica A–300 was used to prepare hydro-compacted nanosilicas cA–300 using various amounts of distilled water in the range of $h$ = 0.5–5.0 g per gram of dry silica. At the maximal amount of water ($h$ = 5 g/g) used here, an individual phase of water (similar to the bulk water) does not form since the system has a gel-like structure. Silica samples with different amounts of added water were carefully stirred and maintained for 3 days in closed dishes at room temperature. Then samples were dried at 450 K for six hours. Note that the samples were appropriately treated before each measurement using a variety of experimental methods.

A FEI Nova NanoSEM (accelerating voltage of 5 kV) scanning electron microscope (SEM)

was used to study the morphology of nanosilica samples. The morphology was also analyzed using a DualBeam Quanta 3D FEG FEI apparatus under conditions of low vacuum at an accelerating voltage of 2–10 kV.

For high-resolution transmission electron microscopy, HRTEM (JEM–2100F, Japan) study, a dried powder sample was added to acetone (for chromatography) and sonicated. Then a drop of the suspension was deposited onto a copper grid with a thin carbon film. After acetone evaporation, sample particles remained on the film were studied with HRTEM.

Small-angle X-ray scattering (SAXS) analysis of initial and hydro-compacted silicas was done using an Empyrean (PANalytical, Netherlands) diffractometer with Cu$K_\alpha$ radiation (with parallel beam X-ray mirror with a W/Si crystal) using a transmission mode with scans over the 0.115 –5° range at a step of 0.01° using a continuous scan mode at 293 K. Before the SAXS measurements, the samples were poured onto a mylar film (6 μm in thickness), leveled and gently kneaded by hand. The beam weakness after passing through the sample was measured, then it was corrected taking into account the background observed calculating the absorption factor of each sample. SAXS patterns were analyzed using PANanalytical EasySAXS V. 2.0.0.405 program (to calculate the particle size distributions (PaSD) with a model of spherical particles) and some approaches using homemade software to calculate the PaSD and pore size distributions (PSD) [50] and other textural characteristics. The differential pore size distribution (PSD) functions $f(r)$ based on the SAXS data were calculated using Fredholm integral equation of the first kind for scattering intensity $I(q)$ [50]

$$I(q) = C\int_{r_{\min}}^{r_{\max}} \frac{\left(\sin qr - qr\cos qr\right)^2}{(qr)^2} V(r) f(r) dr\,, \qquad (1)$$

where $C$ is a constant, $q = 4\pi\sin(\theta)/\lambda$ the scattering vector value, $2\theta$ the scattering angle, $\lambda$ the wavelength of incident X-ray, $V(r)$ the volume of a pore with radius $r$ (proportional to $r^3$), and $f(r)dr$ represents the probability of having pores with radius $r$ to $r + dr$. The values of $r_{\min}$ ($= \pi/q_{\max}$) and $r_{\max}$ ($= \pi/q_{\min}$) correspond to lower and upper limits of the resolvable real space due to instrument resolution. This equation was solved using the CONTIN algorithm [51]. The $f(r)$ function could be converted into incremental PSD (IPSD) $\Phi(r_i) = (f(r_{i+1}) + f_V(r_i))(r_{i+1}-r_i)/2$ for clear view of the PSD at larger $r$ values.

The chord size distribution, $G(r)$ as a geometrical statistic description of a multiphase medium, was calculated from the SAXS data [52, 53]

$$G(r) = C\int_0^\infty \left[K - q^4 I(q)\right] \frac{d^2}{dr^2}\left(-4\frac{\sin qr}{qr}\right) dq\,, \qquad (2)$$

where $K$ is the Porod constant (corresponding to scattering intensity $I(q) \sim Kq^{-4}$ in the Porod range). As a whole, the $G(r)$ function deals with the pore wall thickness and sizes of other nonuniformities with certain boundaries (*e.g.,* proto-particles and nuclei in the NPNP interior) as centers of the X-ray scattering.

The specific surface area based on the SAXS data was calculated (in $m^2/g$) using equation

$$S_{\text{SAXS}} = 10^4 \pi\phi(1-\phi)\frac{K}{Q\rho_a}\,, \qquad (3)$$

where $\phi = \rho_a/\rho_0$ is the solid fraction of adsorbent, and $Q$ is the invariant

$$Q = \int_0^\infty q^2 I(q) dq\,. \qquad (4)$$

The $Q$ value is sensitive to the range used on integration of Eq. (4) (since experimental $q$ values are measured between the $q_{\min}$ and $q_{\max}$ values different from 0 and ∞). Therefore, the invariant value $Q$ was calculated using equation [54]

$$Q = \sum_{q_{\min}}^{q_{\max}} (I(q_i) - b) q_i^2 \Delta q_i + K / q_{\max} \qquad (5)$$

where $b$ is a constant determined using equation

$$I(q)q^4 = K + bq^4 \qquad (6)$$

valid in the Porod range.

To calculate the particle size distribution (PaSD) functions for nanosilica, a model of spherical particles could be applied with integral equation

$$I(q) = C\int_{R_{\min}}^{R_{\max}} P(q,R) f(R) dR\,, \qquad (7)$$

where $C$ is a constant, $R$ is the radius of particles, $f(R)$ is the distribution function (differential

PaSD), and $P(R)$ is the form factor for spherical particles [55] with the kernel $P(q, R) = (4\pi R^3/3)^2[\Phi(q)]^2$ and $\Phi(q,R) = (3/(qR)^3)[\sin(qR) - qR\cos(qR)]$. The PaSD with respect to the volume of particles (as abundance in vol%) could be calculated as follows

$$\text{PaSD(vol\%)} = R^3 f(R) / \int R^3 f(R) dR . \qquad (8)$$

The PaSD could be used to estimate the SAXS SSA using the ratio of the first/zero moments of the first peak in the distribution ($R_{av}$) and the relation between the average size of spherical particles and SSA as follows: $S_{SAXS} = 3/(R_{av}\rho_0)$. Note that the SAXS treatments described above were successfully used for carbon, silica, polymeric and other materials in comparison with the results of various methods used to analyze the nitrogen adsorption, $^1$H NMR cryoporometry data, HRTEM and other methods [40, 56–62].

To analyze the textural characteristics of nanosilicas degassed at 373 K for several hours, low-temperature (77.4 K) nitrogen adsorption–desorption isotherms were recorded using a Micromeritics ASAP 2420 adsorption analyzer. The specific surface area ($S_{BET}$) was calculated according to the standard BET method [63]. Additionally, according to several criteria [49] (*vide infra*), the corrected $S_{BET}$ values (Table 1, $S_{BET,cor}$) were calculated using the corrected surface area occupied by an $N_2$ molecule in the adsorption monolayer $\sigma_m = 0.15$ nm$^2$ (instead of standard 0.162 nm$^2$) in the $p/p_0$ range of 0.05–0.20 (instead of 0.05–0.30), where $p$ and $p_0$ denote the equilibrium and saturation pressure of nitrogen at 77.4 K, respectively. The total pore volume $V_p$ was evaluated from the nitrogen adsorption at $p/p_0 \approx 0.98$–$0.99$ [64]. The incremental PSD were calculated using the density functional theory (DFT) method with a pore model of voids between NPNP (contribution $c_{void}$, Table 1) and cylindrical pores ($c_{cyl}$) (model VC) [65] with a self-consistent regularization (SCR) procedure [66] (DFT VC/SCR method).

The IR spectra of treated and dried nanosilica samples were recorded using a FTIR Thermo Nicolet or a Specord M80 (Carl Zeiss) spectrophotometer. Nanosilica/KBr pellets were prepared with 1:5 or 1:400 ratio using dry KBr powder to record the spectra over the range characteristic for the Si–O stretching vibrations. To record the spectra over the O–H stretching vibrations, thin pellets (pressed at 1500 atm) were prepared without KBr. The IR spectra have been used to estimate the SSA values ($S_{IR}$) from the ratio of the integral intensity of bands of silanols at 3745 cm$^{-1}$ and Si–O overtone at 1870–1860 cm$^{-1}$ [67, 68].

Low-temperature $^1$H NMR spectra of static samples (placed into 4 and 5 mm NMR ampoules) hydrated at $h_{nmr}$ = 1.1 g water per gram of dry silicas A–300 and cA–300 (wetted-treated-dried and preheated at 433 K) were recorded using a Varian 400 Mercury spectrometer (magnetic field 9.4 T, bandwidth 20 kHz) utilizing eight 90° probe pulses of 3 μs duration. Relative mean errors were less than ±10 % for $^1$H NMR signal intensity for overlapped signals, and ±5 % for single signals. Temperature control was accurate and precise to within ±1 K. The accuracy of integral intensities was improved by compensating for phase distortion and zero-line nonlinearity with the same intensity scale at different temperatures. To prevent supercooling of water in samples, the beginning of spectra recording was at 200 K. Samples precooled to this temperature for 10 min were then heated to 285 K at a rate of 5 K/min with steps $\Delta T$ = 10 K or 5 K at a heating rate of 5 K/min for 2 min. They were maintained at a fixed temperature for 5 min, and for data acquisition at each temperature, for 1 min. The applications of the low-temperature $^1$H NMR spectroscopy and NMR cryoporometry, based on the freezing point depression of liquids located in pores dependent on the pore size, to numerous objects were described in detail elsewhere [18, 69–71]. Note that solids (silica, ice) do not contribute the $^1$H NMR spectra of static samples recorded here due to a large difference in the transverse relaxation times of liquid water and immobile components (ice, silica) and due to a narrow bandwidth (20 kHz) of the spectrometer used [18].

## RESULTS AND DISCUSSION

SEM (Fig. 1) and TEM (Fig. 2) images of initial, MCA and hydro-compacted nanosilica, as well as the SSA and $V$ values and other textural characteristics (Table 1, Figs. 3 and 4), and SAXS data (Figs. 3 and 5) demonstrate that the supra-nanoparticulate morphology and texture of cA–300 significantly change *vs*. the hydration degree ($h$). This is due to several processes: (i) destroy of supra-NPNP structures and formation

**Table 1.** Textural characteristics of initial and hydro-compacted A–300 (DFT VC/SCR method)

| $h$ (g/g) | $\rho_b$ (g/cm$^3$) | $S_{BET,cor}$ (m$^2$/g) | $V_p$ (cm$^3$/g) | $\langle R_V \rangle$ (nm) | $\langle R_S \rangle$ (nm) | $S_{nano}$ (m$^2$/g) | $S_{meso}$ (m$^2$/g) | $S_{macro}$ (m$^2$/g) | $V_{nano}$ (cm$^3$/g) | $V_{meso}$ (cm$^3$/g) | $V_{macro}$ (cm$^3$/g) | $c_{void}$ | $c_{cyl}$ |
|---|---|---|---|---|---|---|---|---|---|---|---|---|---|
| 0 | 0.045 | 275 | 0.850 | 30.6 | 8.6 | 94 | 154 | 27 | 0.022 | 0.408 | 0.420 | 0.414 | 0.586 |
| 0.5 | 0.051 | 285 | 0.918 | 40.5 | 9.8 | 97 | 155 | 33 | 0.021 | 0.330 | 0.566 | 0.431 | 0.569 |
| 1.0 | 0.074 | 284 | 1.109 | 39.2 | 11.3 | 86 | 159 | 39 | 0.020 | 0.413 | 0.676 | 0.427 | 0.573 |
| 1.5 | 0.141 | 214 | 1.116 | 44.2 | 14.2 | 57 | 111 | 46 | 0.014 | 0.273 | 0.829 | 0.440 | 0.560 |
| 2.0 | 0.178 | 213 | 1.447 | 22.9 | 12.9 | 55 | 127 | 30 | 0.022 | 0.910 | 0.515 | 0.002 | 0.998 |
| 2.5 | 0.219 | 218 | 1.540 | 22.2 | 13.2 | 55 | 132 | 31 | 0.022 | 1.003 | 0.515 | 0 | 1 |
| 3.0 | 0.238 | 213 | 1.492 | 20.9 | 12.8 | 54 | 134 | 26 | 0.022 | 1.070 | 0.399 | 0 | 1 |
| 4.5 | 0.265 | 220 | 1.488 | 20.4 | 12.9 | 54 | 142 | 23 | 0.022 | 1.128 | 0.339 | 0 | 1 |
| 5.0 | 0.256 | 217 | 1.515 | 21.9 | 13.5 | 54 | 131 | 32 | 0.021 | 1.005 | 0.489 | 0 | 1 |

*Note*. The values of $V_{nano}$ and $S_{nano}$ were calculated by integration of the $f_V(R)$ and $f_S(R)$ functions, respectively, at 0.35 nm ≤ $R$ ≤ 1 nm, $V_{meso}$ and $S_{meso}$ at 1 nm < $R$ ≤ 25 nm, and $V_{macro}$ and $S_{macro}$ at 25 nm < $R$ ≤ 100 nm. The values of $\langle R_V \rangle$ and $\langle R_S \rangle$ as the average pore radii were calculated as a ratio of the first moment of $f_V(R)$ or $f_S(R)$ to the zero moment (integration over the 0.35-100 nm range) $\langle R \rangle = \int f(R) R dR / \int f(R) dR$

**Table 2.** Characteristics of water bound to unmodified A–300 and hydro-compacted cA–300 ($h_{nmr}$ = 1.1 g/g) and related textural characteristics

| $h$ (g/g) | $C_{uw}^s$ (mg/g) | $C_{uw}^w$ (mg/g) | $-\Delta G_s$ (kJ/mol) | $\gamma_S$ (J/g) | $\gamma_S$ (mJ/m$^2$) | $\langle T_m \rangle$ (K) | $S_{nano,uw}$ (m$^2$/g) | $S_{meso,uw}$ (m$^2$/g) | $S_{macro,uw}$ (m$^2$/g) | $V_{nano,uw}$ (cm$^3$/g) | $V_{meso,uw}$ (cm$^3$/g) | $V_{macro,uw}$ (cm$^3$/g) |
|---|---|---|---|---|---|---|---|---|---|---|---|---|
| 0 | 50 | 1050 | 2.58 | 11.55 | 114.4 | 266.1 | 32 | 63 | 6 | 0.014 | 0.790 | 0.085 |
| 1.5 | 75 | 1025 | 2.74 | 14.17 | 116.1 | 264.8 | 48 | 68 | 6 | 0.020 | 0.796 | 0.084 |
| 2.0 | 110 | 990 | 2.88 | 15.39 | 121.2 | 264.4 | 48 | 71 | 8 | 0.020 | 0.819 | 0.105 |
| 3.0 | 170 | 930 | 2.66 | 14.10 | 102.9 | 261.9 | 82 | 53 | 2 | 0.035 | 0.578 | 0.030 |

of new ones (SSA increases then decreases with enhancing hydro-compaction effects, Fig. 3); (ii) decomposition of a surface layer of NPNP at low $h$ values (SSA increases and $G(r)$ changes in the range of small $r$ values, Fig. 5 *d*); (iii) mass-transfer from smaller NPNP toward larger NPNP (SSA decreases, PaSD (Fig. 5 *a*, *b*) and $G(r)$ (Fig. 5 *d*) change) and compaction of the pore walls (contribution of cylindrical pores (Table 1, $c_{cyl}$) becomes dominant) at high $h$ values; and (iv) strong reorganization of the supra-NPNP structures (Table 1, Figs. 1–5). The secondary structures (NPNP aggregates, Figs. 1 *c* and 2 *d*), as well ternary structures with agglomerates (Fig. 2 *c*), become denser after hydro-compaction of nanosilica (Figs. 1 and 2, Table 1, $\rho_b$). The MCA treatment of dry A–300 results in the decomposition of large aggregates, but the aggregates with several NPNP could remain, and free small NPNP appear (Fig. 2 *b*). Similar results could be upon the hydro-compaction of A–300 at low values of $h \le 1.0$ g/g because the SSA value increases in comparison to that of initial A–300 (Table 1, Fig. 3).

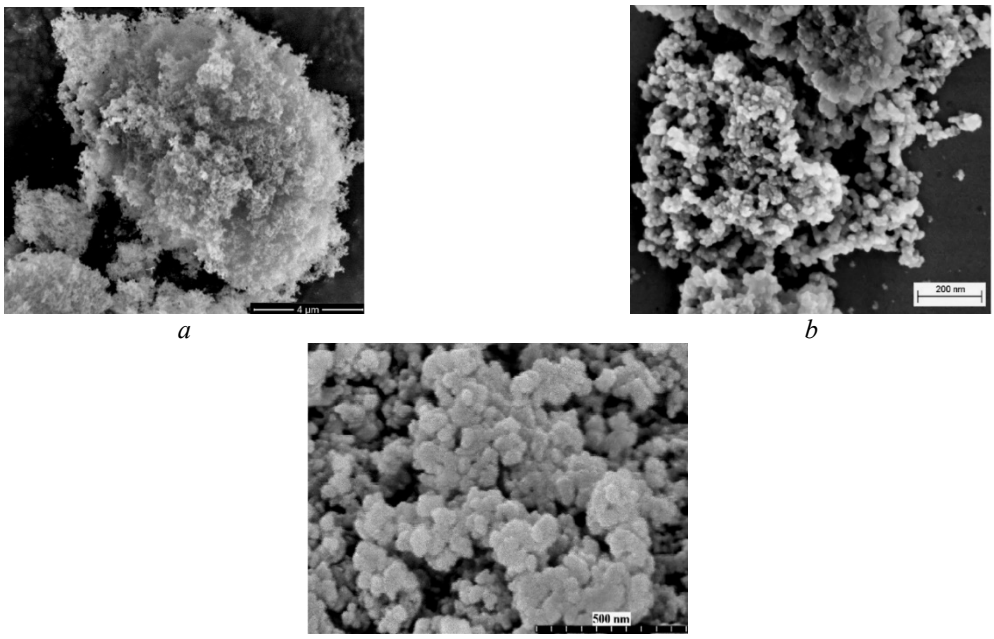


*a* *b* *c*

**Fig. 1.** SEM images of A–300 (*a*, *b*) initial and (*c*) hydro-compacted at water content $h$ = 3 g/g and then dried (scale bars: (*a*) 4 μm, (*b*) 200 nm, and (*c*) 500 nm)

The difference in the SAXS PaSD computed using firm (Fig. 5 *a*) and developed (Fig. 5 *b*) software is due to the use of a smaller value of the regularization parameter (α) for the latter. This has been done to distinguish the structures related to individual NPNP (the first peak at $d \approx 10$ nm, Fig. 5 *b*) and supra-NPNP (all other peaks). Changes in the PaSD peak positions and intensity *vs.* $h$ values (Fig. 5 *b*) occur due to several processes: (i) partial decomposition of aggregates (the second and subsequent peaks shift toward smaller $d$ values or/and their intensity decreases); (ii) destroy of surface layers of NPNP (first peak shifts toward smaller $d$ values, and intensity of $G(r)$ decreases at small values $r \le 1$ nm, Fig. 5 *d*); (iii) the reorganization of the supra-NPNP structures suggesting by changes in PaSD (Fig. 5), PSD (Fig. 4), other textural characteristics (Table 1, Fig. 3) and particulate morphology (Figs. 1 and 2). Note that not only wetting-stirring but also subsequent drying can strongly affect the supra-NPNP structures [18–22, 47, 48]. The reorganization of the supra-NPNP structures *vs*. the $h$ value is well visible from non-monotonic changes in the values of the average pore radii $\langle R_V \rangle$ and $\langle R_S \rangle$ (Fig. 3) with respect to the pore volume and SSA, as well as from changes in other textural characteristics (Table 1, Figs. 3–5).

As a whole, the results of the analyses of the SAXS data and nitrogen adsorption-desorption

isotherms (Table 1, Figs. 3–5) are in agreement with microscopic images (Figs. 1 and 2). However, there are some additional factors, which should be considered upon the analysis of the textural characteristics of treated nanosilicas. First, the empty volume in the nanosilica powder ($V_{em} = 1/\rho_b - 1/\rho_0$, where $\rho_b$ and $\rho_0$ are the bulk and true densities of samples, respectively) is much greater than the $V_p$ value of adsorbed nitrogen even at $p/p_0 = 0.999$. For example, $V_{em} = 21.8$ cm$^3$/g for initial A–300 at $\rho_b = 0.045$ g/cm$^3$, but the value of $V_p$ is much smaller (Table 1). This underestimation of the value of $V_p$ calculated from the nitrogen adsorption is due to very weak influence of the pore walls (nanoparticle surface) on the nitrogen molecules located in macropores far from a solid surface in loose supra-NPNP structures. After hydro-compaction of A–300, the difference between the values of $V_{em}$ and $V_p$ strongly decreases, *e.g.*, $V_{em} = 3.45$ cm$^3$/g and $V_p = 1.49$ cm$^3$/g for cA–300 treated at $h = 4.5$ g/g. Therefore, the PSD (Fig. 4 *b*) can describe only a part of voids between NPNP in secondary/ternary structures, and these parts differ for PSD based on the data of other methods (*e.g.*, SAXS and cryoporometry) due to their features [18, 40]. For example, the curves of the SSA values *vs. h* differ for a set of used methods (Fig. 3 *a*); however, they have similar shapes with larger SSA values at smaller *h* and smaller SSA values at larger *h* values.

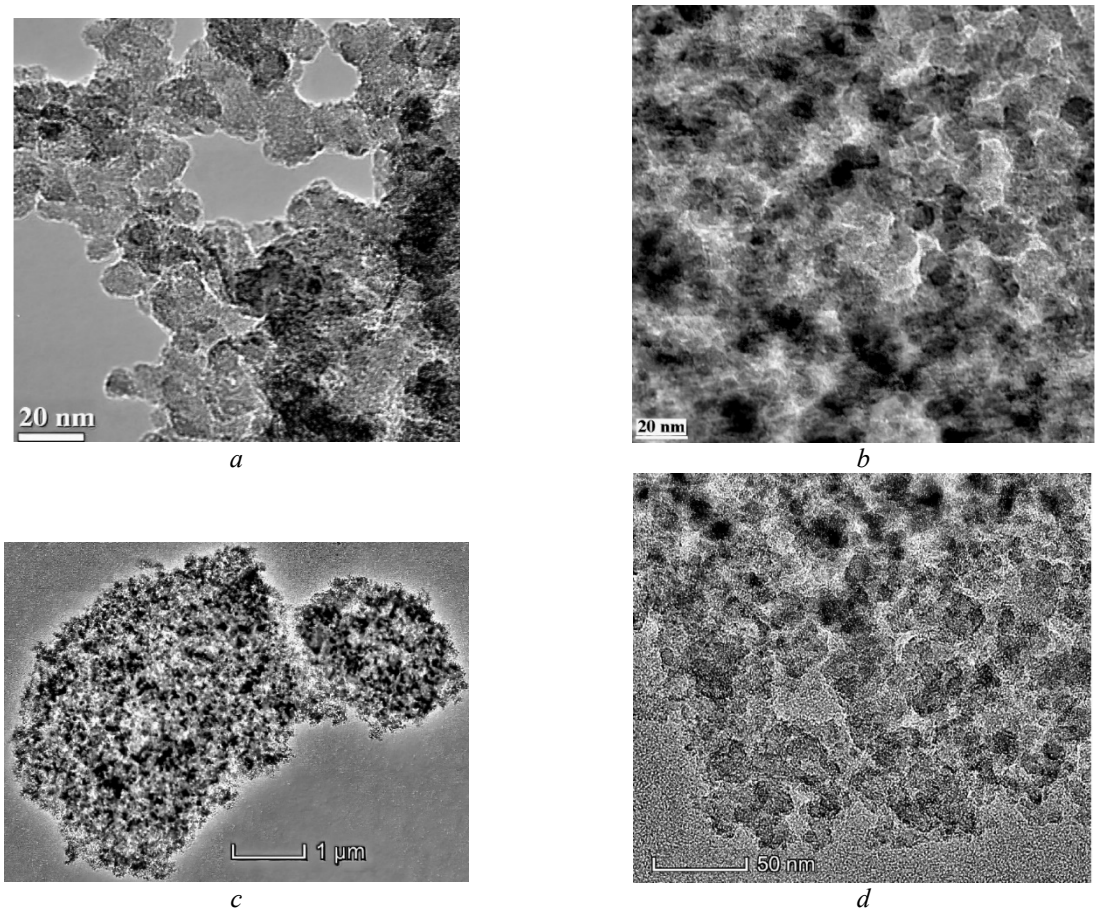


*a* *b* *c* *d*

**Fig. 2.** TEM images of A–300 (*a*) initial, (*b*) MCA of the dry powder, (*c*, *d*) hydro-compacted at $h = 3$ g/g and then dried (scale bar (*a*, *b*) 20 nm, (*c*) 1 μm, and (*d*) 50 nm)

According to SAXS IPSD (Fig. 5 *c*) contribution of nanopores slightly increases with increasing *h* value, as well as a contribution of narrow mesopores at 1 nm < $R \le 10$ nm. However, the main peak corresponds to broad mesopores similar to that for DFT VC/SCR pores (Fig. 4 *d*). Note that SAXS can give information on pores inaccessible for nitrogen molecules. Therefore, contribution of narrow pores in the SAXS IPSD (Fig. 5 *c*) is greater than that in the DFT VC/SCR

IPSD (Fig. 4 *b*). Both DFT VC/SCR IPSD (Fig. 4 *b*) and SAXS IPSD (Fig. 5 *c*), demonstrate an enhanced contribution of broad meso/macropores at 10 nm < $R$ ≤ 30 nm with increasing $h$ value. Note that the pore shape changes with increasing $h$ since a contribution of cylindrical pores becomes predominant at $h \geq 2$ g/g (Table 1, $c_{void}$ and $c_{cyl}$). Additionally, the chord size distribution (Fig. 5 *d*), which could be considered as a pore wall thickness or the thickness of some structures in the NPNP interior (*e.g.*, nuclei and proto-particles), changes *vs.* $h$ value. The sizes of these structures could be estimated using SAXS, HRTEM, and XRD [72] giving sizes in the range of 0.5–2.0 nm. These values are in agreement with the chord values at $r \leq 2$ nm (Fig. 5 *d*).

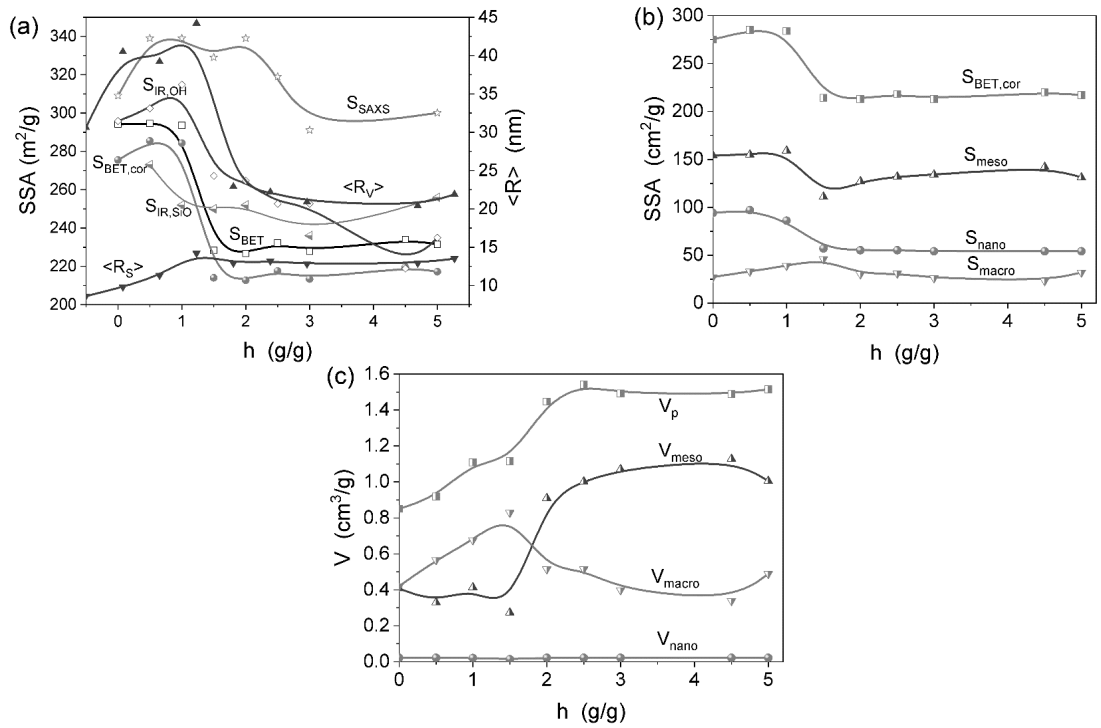


**Fig. 3.** (*a*) The specific surface area estimated from nitrogen adsorption (standard $S_{BET}$ and corrected $S_{BET,cor}$), SAXS data as the ratio of the first / zero moments of the first peak of the PaSD ($S_{SAXS}$), IR spectra using the ratio of the integral intensity of bands of silanols at 3750–3745 cm$^{-1}$ and Si–O overtone at 1870–1860 cm$^{-1}$ ($S_{IR,OH}$) and integral intensity of two modes of Si–O at 1200 cm$^{-1}$ (surface) and 1100 cm$^{-1}$ (bulk) ($S_{IR,SiO}$) *vs*. the water amount used on silica hydro-compaction; (*b*) $S_{BET,cor}$ and nano- (0.35 nm ≤ $R$ ≤ 1 nm), meso- (1 nm < $R$ ≤ 25 nm), and macro- (25 nm < $R$ ≤ 100 nm) components *vs.* $h$; and (*c*) $V_p$ and components *vs.* $h$

A complex picture is observed for the SAXS IPSD (Fig. 5 *c*) in the range of broad mesopores, as well as for macropores at $R$ > 25 nm, *vs*. the $h$ value. Additionally, at small $R$ values, it is possible X-ray scattering on proto-particles and nuclei located in the NPNP interior [72]. The DFT VC/SCR method giving a clearer picture related only to pores accessible for nitrogen molecules adsorbed (Fig. 4 *d*) than SAXS IPSD (Fig. 5 *c*) shows that the maximal contribution of macropores (Table 1, $V_{macro}$, $S_{macro}$) is observed in a middle range of $h$ = 1–2 g/g with a maximum for macropores at $h$ = 1.5 g/g (Fig. 3). Sample cA–300 prepared at $h$ = 1.5 g/g corresponds to the first sample with the water amount greater than $V_p$ of cA–300. It is the first one with partially collapsed secondary structure since a significant decrease in the value of SSA (Table 1, Fig. 3) is observed. However, the value of $\rho_b$ is middle at $h$ = 1.5 g/g and it continue grows with increasing $h$ to 4.5 g/g (Table 1).

The estimations of the SSA (Fig. 3) using the SAXS PaSD or IR spectra (Fig. 3) confirm that the value of $h$ = 1.5 g/g is a critical one for reorganization of the supra-NPNP structures. Note that the $S_{SAXS}$ values are larger than $S_{BET}$

because the former corresponds to total surface area, a part of which is inaccessible for the probe $N_2$ molecules. Additionally, the SAXS SSA values estimated from PaSD (Fig. 3) or using Eq. (3) are similar, *e.g.*, for initial A–300, it is equal to 309 and 311 $m^2/g$, respectively.

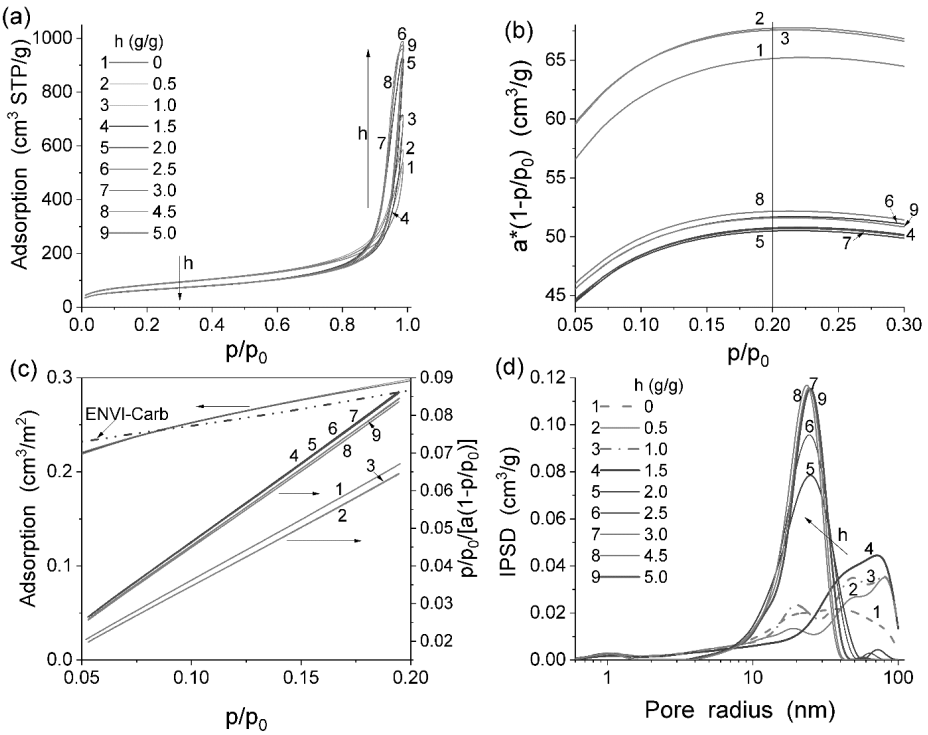


**Fig. 4.** (*a*) Nitrogen adsorption-desorption isotherms for initial and compacted nanosilica samples; (*b*) reduced adsorption isotherms used to estimate an appropriate $p/p_0$ range (to calculate the $S_{BET}$ values) corresponding to continuous increasing reduced adsorption as $a\times(1 - p/p_0)$ giving the appropriate range at $p/p_0 = 0.05–0.20$); (*c*) adsorption isotherms per $m^2$ (adsorption in $cm^3/g$ is divided by $S_{BET,cor}$) compared to that for graphitized carbon black ENVI-Carb (Supelco) [49] and linearized BET plots for nanosilicas; and (*d*) incremental pore size distributions (DFT VC/SCR method)

Certain structural changes in cA–300 are already observed at low $h$ values (Figs. 3–5, Table 1). It is possible that these changes at small $h$ values are due to complex treatment with wetting-stirring-aging-drying. These textural changes features can be explained by the clustered adsorption of water, *i.e.*, it can be located in contact zones between adjacent NPNP. The amount of water at $h \geq 0.5$ g/g is much greater than the volume of nanopores (Table 1, $V_{nano}$). This is of importance since water tends to be located in narrower pores and narrow voids correspond to contact area between neighboring NPNP. Therefore, water can stimulate reorganization of contacts between neighboring NPNP in their aggregates up to decomposition of the supra-NPNP structures upon stirring. This reorganization leads to an increase in the accessibility of the NPNP surface (after drying and degassing) for nitrogen molecules and accessible SSA increases (Table 1, Fig. 3). This effect is stronger at $h$ = 0.5–1.0 g/g because the supra-NPNP structures are destroyed but the water amounts are not enough to reorganize these structures as it is observed at higher $h$ values.

Some information on the behavior of the supra-NPNP structures of cA–300 additionally wetted could be obtained using low-temperature $^1$H NMR spectroscopy of static samples and NMR cryoporometry with water as a probe adsorbate [18]. In the $^1$H NMR spectra of water (fixed hydration at $h_{nmr}$ = 1.1 g/g) bound to A–300 and cA–300 (Fig. 6), there is single, slightly asymmetrical signal at the chemical shift of proton resonance $\delta_H \approx 5$ ppm close to that of bulk water [18]. Its intensity diminishes with lowering temperature due to step-by-step freezing-out of bound water with decreasing temperature

$T < 273$ K. A fraction of water frozen at $T < 260$ K may be attributed to strongly bound water (SBW) (Fig. 7). Water frozen at 260 K ≤ $T$ ≤ 273 K corresponds to weakly bound water (WBW) [18]. The amounts of unfrozen water ($C_{uw}$) *vs*. $T$ (Fig. 7 *a*) could be used to estimate the size distribution of pores filled by unfrozen water at $T$ < 273 K (Fig. 8) using the Gibbs–Thomson relation for the freezing/melting point depression of water (or other liquids confined in pores) depending on the pore sizes. These distributions could be used to estimate a part of pores containing unfrozen water (Table 2).

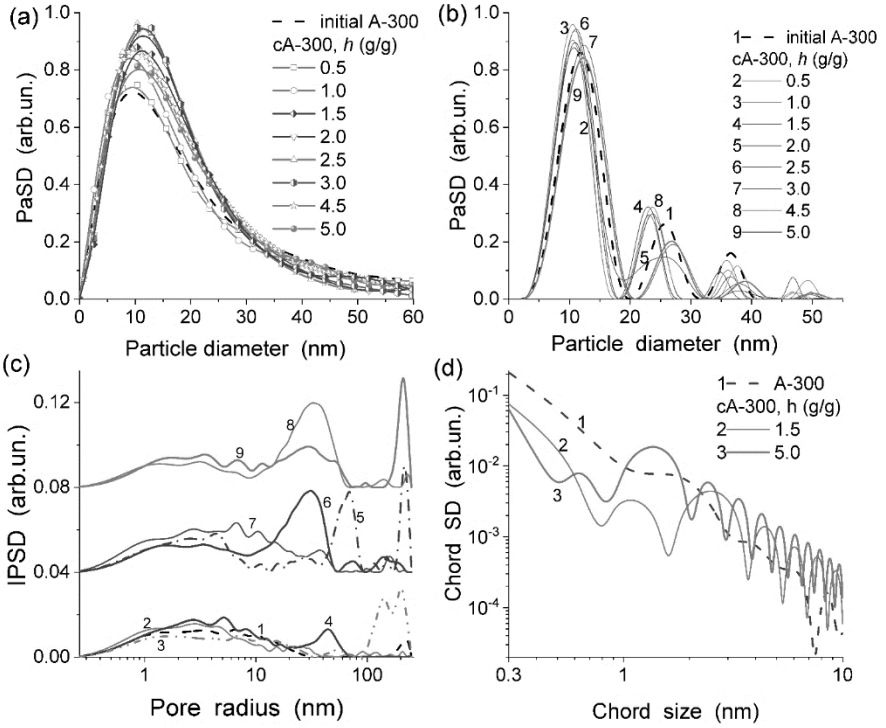


**Fig. 5.** Particle size distributions (PaSD) for initial and hydro-compacted nanosilica calculated using the SAXS patterns analyzed with (*a*) firm and (*b*) developed software using Eqs. (7) and (8); (*c*) incremental pore size distributions (IPSD) calculated with Eq. (1); and (*d*) chord size distributions for selected samples computed using Eq. (2) in the Porod range at $q \approx 0.5$–$2.0$ (1/nm)

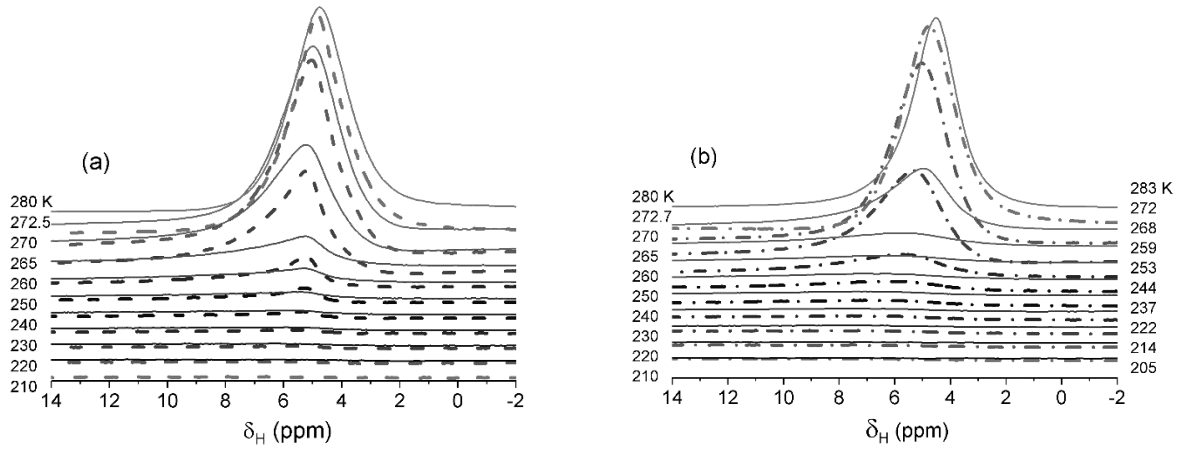


**Fig. 6.** $^1$H NMR spectra (recorded at different temperatures upon heating from minimal one used) of water (1.1 g/g) adsorbed on a surface of nanosilica A–300 (*a*) initial (dashed lines) and hydro-compacted at $h$ = (*a*) 1.5 g/g (solid lines) and (*b*) 2.0 g/g (dot-dashed lines) and 3.0 g/g (solid lines)

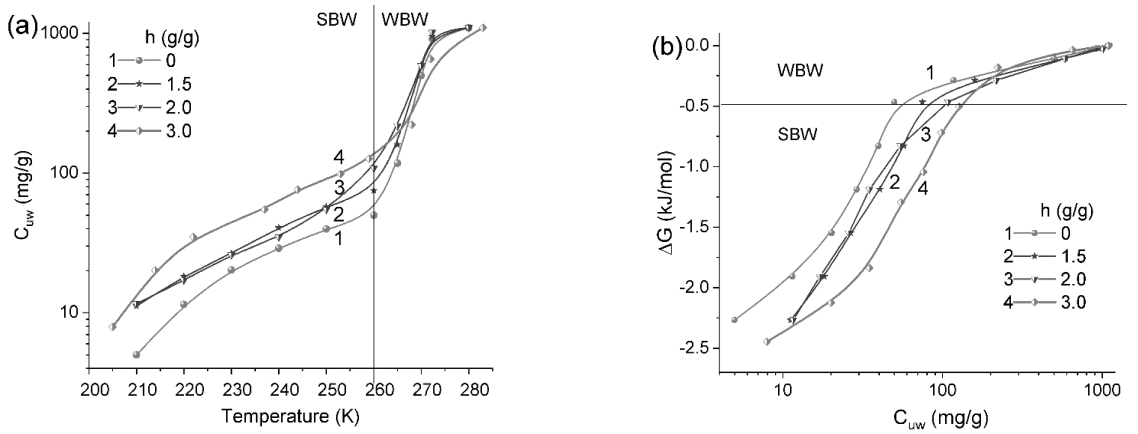


**Fig. 7.** (*a*) Temperature dependences of the content of unfrozen water ($C_{uw}$) estimated from integral intensity of the $^1$H NMR spectra recorded at different temperatures, and (*b*) changes in the Gibbs free energy $\Delta G$ *vs*. $C_{uw}$ for A–300 and cA–300 (hydro-compacted at $h$ = 1.5, 2, and 3 g/g) with constant hydration upon the NMR measurements at $h_{nmr}$ = 1.1 g/g

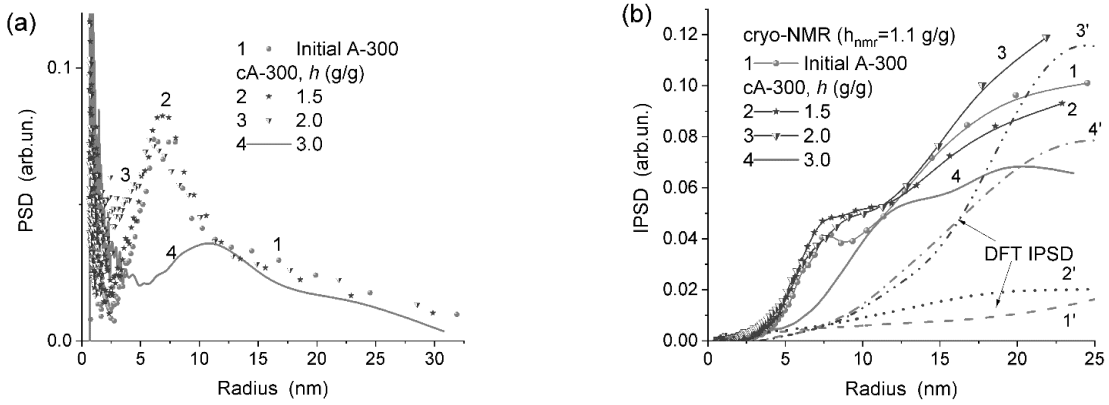


**Fig. 8.** Size distributions of unfrozen water structures filling voids between NPNP (*a*) differential (PSD) and (*b*) incremental (IPSD) calculated using NMR cryoporometry method (at constant $h_{nmr}$ = 1.1 g/g) applied to initial A–300 and cA–300 at different $h$ values (dot-dashed lines 1', 2', 3', and 4' correspond to DFT VC/SCR)

The amount of water in samples studied using the $^1$H NMR spectroscopy was constant at $h_{nmr}$ = 1.1 g/g that is smaller than $V_p$ of cA–300, but it is greater than $V_p$ of initial A–300 and slightly smaller than the critical content of water strongly affecting the reorganization of the supra-NPNP structures (Table 1). The amount of SBW (a fraction of $h_{nmr}$) increases with increasing degree of wetting upon the hydro-compaction of silica (Table 2, $C_{uw}^s$). This leads to a decrease in the average melting temperature $<T_m>$. There is a tendency in increasing values of $-\Delta G_s$ (Gibbs free energy related to SBW) and $\gamma_S$ (related to all bound water) with increasing hydration upon the hydro-compaction (Table 2) due to changes in the topology of pores (Fig. 3–5). The mentioned effects are due to an increase in contribution of nanopores filled by unfrozen water (Table 2, $S_{nano,uw}$, $V_{nano,uw}$). Note that $V_{nano,uw} > V_{nano}$ at $h$ = 3 g/g and $V_{meso,uw} > V_{meso}$ at $h$ = 0 and 1.5 g/g (Tables 1 and 2) due to the reorganization of the supra-NPNP structures after additional wetting.

A relative contribution (with respect to the value of $S_{BET,cor}$) of contact area of unfrozen water with a silica surface increases with increasing $h$, *e.g.*, from 36.7 % (A–300) to 64.3 % (cA–300 compacted at $h$ = 3 g/g). However, a contribution of filled mesopores is maximal at $h$ = 2 g/g and it decreases at $h$ = 3 g/g (Table 2, $V_{meso,uw}$, $S_{meso,uw}$, Fig. 8) due to changes in the PSD upon enhanced hydro-compaction (Fig. 4 *d*). A contribution of macropores filed by unfrozen water is small (Table 2, $V_{macro,uw}$, $S_{macro,uw}$) because the amount of

adsorbed water was relatively small ($h_{nmr}$ = 1.1 g/g) and much smaller than $V_{em}$ and $V_p$ of cA–300 studied (Table 1). Therefore, adsorbed water is mainly located in nano/mesopores. At $h$ = 2 and 3 g/g, DFT VC/SCR IPSD and NMR IPSD (Fig. 8 *b*) are closer than that for initial A–300 and cA–300 compacted at $h$ = 1.5 g/g. This result can be explained by a greater reorganization of cA–300 prepared at $h$ = 1.5 g/g or initial A–300 after additional wetting ($h_{nmr}$ = 1.1 g/g) and equilibration of the system before the $^1$H NMR measurements. Additionally, the differences in the PSD of these samples (Fig. 4 *d*) could play an important role upon the second wetting. Thus, one can conclude that wetting and drying of nanosilica under relatively soft conditions can reduce the dusting effect (since the bulk density strongly increases up to 0.27 g/cm$^3$ instead of 0.05 g/cm$^3$ for the initial powder) quite characteristic for the initial nanosilica. However, it is remained certain activity in the reorganization of the supra-NPNP structures upon additional wetting. This is of importance because many practical applications of fumed silicas deal with the activity of individual NPNP or their small aggregates, and the formation of large rigid supra-NPNP structures as in xerogels (*e.g.*, Silochrome) or silica gels could be considered as rather negative results.

## CONCLUSION

The hydro-compaction effects for nanosilica A–300 under standard conditions depend strongly on the amounts of water (in the range of 0.5–5.0 g/g) used in the processes with wetting-stirring-drying. A selection of a certain amount of water upon the hydro-compaction allows one to provide an appropriate reorganization of the supra-NPNP structures. This is accompanied by certain changes in the morphological (PaSD, $G(r)$) and textural characteristics ($S$, $V$, PSD) of the dried materials. However, according to TEM and SAXS data, the nanoparticles *per se* are weakly affected by the hydro-compaction, *i.e.*, the rearrangement of the supra-NPNP structures is predominant upon the nanosilica hydro-compaction studied here. At a low degree of wetting ($h \le 1$ g/g), the textural reorganization and morphological changes of cA–300 do not lead to reduction of the specific surface area. The SSA even slightly increases due to the decomposition of the NPNP aggregates. However, at $h \ge 1.5$ g/g, the SSA decreases, but the pore volume (nitrogen adsorption at $p/p_0 \approx 0.99$) increases despite the empty volume of the powder decreases from 21.8 cm$^3$/g for initial A–300 ($\rho_b$ = 0.045 g/cm$^3$) to 3.45 cm$^3$/g after hydro-compaction at $h$ = 4.5 g/g ($\rho_b$ = 0.256 g/cm$^3$). Note that the structural reorganization of the dried hydro-compacted cA–300 powders is possible upon repeated wetting. This suggests that the chemical bonds between adjacent NPNP do not practically form in cA–300 upon the hydro-compaction and drying under soft conditions. Thus, hydro-compacted nanosilica loses the dust-forming property (since the bulk density strongly increases) but remains active with respect to the NPNP activity and mobility due to decomposition of the supra-NPNP structures, *e.g.*, in aqueous or other liquid media. This is of importance for practical applications of nanosilicas, especially in aqueous suspensions, in drug delivery systems, upon filling of polymers, *etc.*

## ACKNOWLEDGEMENT

The authors are grateful to the National Research Foundation of Ukraine ("Support of advanced and young scientists", grant 2020.02/0057) for financial support of the study. The authors thank Prof. R. Leboda, Dr. J. Skubiszewska-Zięba, and Dr. B. Charmas (Maria Curie-Sklodowska University, Lublin, Poland) for a set of raw experimental data.

# Морфологія частинок та текстурні характеристики нанокремнезему, гідро-ущільненого при різних ступенях гідратації

**В.М. Гунько, В.В. Туров**

*Інститут хімії поверхні ім. О.О. Чуйка Національної академії наук України*
*вул. Генерала Наумова, 17, Київ, 03164, Україна, vlad_gunko@ukr.net*

*Морфологію часинок та текстурні характеристики нанокремнезему А–300, вихідного та гідро-ущільненого (сА–300, змочений водою у різній кількості у діапазоні h = 0.5–5.0 г на грам сухого кремнезему, механічно тренований і потім висушений), було проаналізовано з використанням низько-температурної ЯМР $^1$H спектроскопії (треновані-висушені-змочені зразки), мало-кутового розсіяння рентгенівських променів, скануючої та трансмісійної електронної мікроскопії, інфрачервоної спектроскопії та адсорбції азоту (треновані-висушені-дегазовані зразки). Результати гідро-ущільнення нанокремнезему А–300 сильно залежать від величини h. Цей параметр можна змінювати для контролю реорганізації агрегатів непористих наночастинок (НПНЧ, що складаються зі щільно упакованих проточастинок чи зародків) та агломератів агрегатів (вторинні та третинні структури відповідно), як і видимих частинок (тобто є п'яти-рівнева ієрархія структур нанокремнезема з три-рівневою супра-НПНЧ структурою). Ущільнення супроводжується немонотонними змінами морфологічних та текстурних характеристик сА–300. Наночастинки зазнають значно менших змін на відміну супра-НПНЧ структур. При h ≤ 1 г/г реорганізація супра-НПНЧ структур не призводить до зменшення питомої поверхні ($S_{БЕТ}$); проте при h ≥ 1.5 г/г величина $S_{БЕТ}$ зменшується, але об'єм пор зростає попри те, що пустий об'єм у порошку зменшується з 21.8 см$^3$/г для вихідного А–300 (насипна густина $\rho_b$ = 0.045 г/см$^3$) до 3.45 см$^3$/г при ущільненні при h = 4.5 г/г ($\rho_b$ = 0.256 г/см$^3$). Текстурна реорганізація гідро-ущільненого нанокремнезему можлива і при повторному змочуванню. Це свідчить про те, що хімічні зв'язки між сусідніми НПНЧ практично не утворюються при гідро-ущільненні та наступній сушці. Тобто, гідро-ущільнений нанокремнезем втрачає здатність пилоутворення, але залишається активним щодо рухливості НПНЧ, наприклад, у водному середовищі, та зберігається можливість реорганізації супра-НПНЧ структур під дією зовнішніх чинників, що має певне практичне значення.*

***Ключові слова**: гідро-ущільнений нанокремнезем, змочений нанокремнезем, морфологія частинок, текстурні характеристики, реорганізація структурної ієрархії*

REFERENCES

1. Hastie J.W. *Materials Chemistry at High Temperatures*. V. 1. *Characterization*. V. 2. *Processing and Performance*. (Clifton, New York: Humana Press, 1990).
2. *Ullmann's Encyclopedia of Industrial Chemistry*. (Weinheim: Wiley-VCH, 2008).
3. Bhushan B. *Encyclopedia of Nanotechnology*. (Dordrecht: Springer, 2012).
4. *Basic characteristics of Aerosil fumed silica* (4th ed.) Tech. Bull. Fine Particles 11. (Hanau: Evonik Industries, 2014).
5. Kulkarni P., Baron P.A., Willeke K. *Aerosol Measurement: Principles, Techniques, and Applications*. Third Edition. (New York: John Wiley & Sons, 2011).
6. Büchel K.H., Moretto H.-H., Woditsch P. *Industrial Inorganic Chemistry*. (Weinheim: Wiley-VCH, 2000).
7. Xu R., Yan Xu Y. *Modern Inorganic Synthetic Chemistry*. (Elsevier: Amsterdam, 2017).
8. Auner N., Weis J. *Oganosilicon Chemistry VI*. (Weinheim: Wiley-VCH Verlag GmbH, 2005).
9. Mueller R., Madler L., Pratsinis S.E. Nanoparticle synthesis at high production rates by flame spray pyrolysis. *Chem. Eng. Sci*. 2003. **58**(10): 1969.
10. Camenzind A., Caseri W.R., Pratsinis S.E. Flame-made nanoparticles for nanocomposites. *Nano Today*. 2010. **5**(1): 48.
11. Teoh W.Y., Lutz M. Flame spray pyrolysis: An enabling technology for nanoparticles design and fabrication. *Nanoscale*. 2010. **2**(8): 1324.
12. Ensor D.S. *Aerosol Science and Technology: History and Reviews*. (Research Triangle Park, NC: RTI Press, 2011).
13. Babick F. *Suspensions of Colloidal Particles and Aggregates*. (Berlin: Springer, 2018).

14. Iler R.K. *The Chemistry of Silica. Solubility, Polymerization, Colloid and Surface Properties, and Biochemistry*. (Chichester: Wiley, 1979).
15. Bergna H.E., Roberts W.O. *Colloidal Silica: Fundamentals and Applications*. (Boca Raton: CRC Press, 2006).
16. Somasundaran P. *Encyclopedia of Surface and Colloid Science*. Third Edition. (Boca Raton: CRC Press, 2015).
17. Legrand A.P. *The Surface Properties of Silicas*. (New York: Wiley, 1998).
18. Gun'ko V.M., Turov V.V. *Nuclear Magnetic Resonance Studies of Interfacial Phenomena*. (Boca Raton: CRC Press, 2013).
19. Gun'ko V.M., Zarko V.I., Leboda R., Chibowski E. Aqueous suspensions of fumed oxides: particle size distribution and zeta potential. *Adv. Colloid Interface Sci.* 2001. **91**(1): 1.
20. Gun'ko V.M., Turov V.V., Zarko V.I., Goncharuk O.V., Pahklov E.M., Skubiszewska-Zięba J., Blitz J.P. Interfacial phenomena at a surface of individual and complex fumed nanooxides. *Adv. Colloid Interface Sci.* 2016. **235**: 108.
21. Gun'ko V.M., Turov V.V., Goncharuk O.V., Pakhlov E.M., Matkovsky O.K. Interfacial phenomena at a surface of individual and complex fumed nanooxides. *Surface*. 2019. **11(26)**: 3.
22. Gun'ko V.M., Turov V.V., Zarko V.I., Pakhlov E.M., Charmas B., Skubiszewska-Zięba J. Influence of structural organization of silicas on interfacial phenomena. *Colloids Surf. A*. 2016. **492**: 230.
23. Atkins D., Kékicheff P., Spalla O. Adhesion between colloidal silica as seen with direct force measurement. *J. Colloid Interface Sci.* 1997. **188**(1): 234.
24. Ding P., Orwa M.G., Pacek A.W. De-agglomeration of hydrophobic and hydrophilic silica nano-powders in a high shear mixer. *Powder Technol*. 2009. **195**(3): 221.
25. Dekkers S., Krystek P., Peters R.J.B., Lankveld D.P.K., Bokkers B.G.H., Van Hoeven-Arentzen P.H., Bouwmeester H., Oomen A.G. Presence and risks of nanosilica in food products. *Nanotoxicology*. 2011. **5**(3): 393.
26. Taylor P., Chen H., Zhou S., Gu G., Wu L. Modification and dispersion of nanosilica. *J. Dispersion Sci. Technol.* 2008. **25**(6): 837.
27. Biricik H., Sarier N. Comparative study of the characteristics of nano silica–, silica fume– and fly ash – incorporated cement mortars. *Mater. Res.* 2014. **17**(3): 570.
28. Napierska D., Thomassen L.C.J., Lison D., Martens J.A., Hoet P.H. The nanosilica hazard: another variable entity. *Part. Fibre Toxicol.* 2010. **7**(39): 1.
29. Hashim A.A. *Smart Nanoparticles Technology*. (Rijeka, Croatia: InTech, 2012).
30. Irfan A., Cauchi M., Edmands W., Gooderham N.J., Njuguna J., Zhu H. Assessment of temporal dose-toxicity relationship of fumed silica nanoparticle in human lung A549 cells by conventional cytotoxicity and $^{1}$H-NMR-based extracellular metabonomic assays. *Toxicol. Sci*. 2014. **138**(2): 354.
31. Eom H.-J., Choi J. Oxidative stress of silica nanoparticles in human bronchial epithelial cell, Beas-2B. *Toxicol In Vitro.* 2009. **23**(7): 1326.
32. Chang J.-S., Chang K.L.B., Hwang D.-F., Kong Z.-L. In vitro cytotoxicitiy of silica nanoparticles at high concentrations strongly depends on the metabolic activity type of the cell line. *Environ. Sci. Technol*. 2007. **41**(6): 2064.
33. Brunner T.J., Wick P., Manser P., Spohn P., Grass N., Limbach L.K., Bruinink A., Stark W.J. In vitro cytotoxicity of oxide nanoparticles: comparison to asbestos, silica, and the effect of particle solubility. *Environ. Sci. Technol*. 2006. **40**(14): 4374.
34. Koduru J.R., Karri R.R., Mubarak N.M., Bandala E.R. *Sustainable Nanotechnology for Environmental Remediation*. (Amsterdam: Elsevier, 2022).
35. Bhat R. *Valorization of Agri-Food Wastes and By-Products. Recent Trends, Innovations and Sustainability Challenges*. (Amsterdam: Elsevier, 2021).
36. Iqbal H., Bilal M., Nguyen T.A., Yasin G. *Biodegradation and Biodeterioration at the Nanoscale*. (Amsterdam: Elsevier, 2021).
37. Fu Q., Zhao X., Zhang Z., Xu W., Niu D. Effects of nanosilica on microstructure and durability of cement-based materials. *Powder Technol.* 2022. **404**: 117447.
38. Laím L., Caetano H., Santiago A. Review: Effects of nanoparticles in cementitious construction materials at ambient and high temperatures. *J. Build. Eng*. 2021. **35**: 102008.
39. Rigby S.P., Fairhead M., van der Walle C.F. Engineering silica particles as oral drug delivery vehicles. *Curr. Pharm. Des*. 2008. **14**(18): 1821.
40. Gun'ko V.M., Turov V.V., Pakhlov E.M., Krupska T.V., Charmas B. Effect of water content on the characteristics of hydro-compacted nanosilica. *Appl. Surf. Sci*. 2018. **459**: 171.
41. Gun'ko V.M., Turov V.V., Zarko V.I., Pakhlov E.M., Prykhod'ko G.P., Remez O.S., Leboda R., Skubiszewska-Zięba J., Blitz J.P. High-pressure cryogelation of nanosilica and surface properties of cryosilicas. *Colloids Surf. A*. 2013. **436**: 618.

42. Gun'ko V.M., Turov V.V., Zarko V.I., Pakhlov E.M., Matkovsky A.K., Oranska O.I., Palyanytsya B.B., Remez O.S., Nychiporuk Y.M., Ptushinskii Y.G., Leboda R., Skubiszewska-Zięba J. Cryogelation of individual and complex nanooxides under different conditions. *Colloids Surf. A*. 2014. **456**: 261.
43. Gun'ko V.M., Zarko V.I., Pakhlov E.M., Matkovsky A.K., Remez O.S., Charmas B., Skubiszewska-Zięba J. Low-temperature high-pressure cryogelation of nanooxides. *J. Sol-Gel Sci. Technol*. 2015. **74**(1): 45.
44. Gun'ko V.M., Skubiszewska-Zięba J., Leboda R., Khomenko K.N., Kazakova O.A., Povazhnyak M.O., Mironyuk I.F. Influence of morphology and composition of fumed oxides on changes in their structural and adsorptive characteristics on hydrothermal treatment at different temperatures. *J. Colloid Interface Sci*. 2004. **269**(2): 403.
45. Gun'ko V.M. Interfacial phenomena: effects of confined space and structure of adsorbents on the behavior of polar and nonpolar adsorbates at low temperatures. *Curr. Phys. Chem*. 2015. **5**(2): 137.
46. Gun'ko V.M., Mironyuk I.F., Zarko V.I., Voronin E.F., Turov V.V., Pakhlov E.M., Goncharuk E.V., Nychiporuk Yu.M., Kulik T.V., Palyanytsya B.B., Pakhovchishin S.V., Vlasova N.N., Gorbik P.P., Mishchuk O.A., Chuiko A.A., Skubiszewska-Zięba J., Janusz W., Turov A.V., Leboda R. Morphology and surface properties of fumed silicas. *J. Colloid Interface Sci*. 2005. **289**(2): 427.
47. Gun'ko V.M., Voronin E.F., Nosach L.V., Turov V.V., Wang Z., Vasilenko A.P., Leboda R., Skubiszewska-Zięba J., Janusz W., Mikhalovsky S.V. Structural, textural and adsorption characteristics of nanosilica mechanochemically activated in different media. *J. Colloid Interface Sci.* 2011. **355**(2): 300.
48. Gun'ko V.M., Voronin E.F., Zarko V.I., Goncharuk E.V., Turov V.V., Pakhovchishin S.V., Pakhlov E.M., Guzenko N.V., Leboda R., Skubiszewska-Zięba J., Janusz W., Chibowski S., Chibowski E., Chuiko A.A. Interaction of poly(vinyl pyrrolidone) with fumed silica in dry and wet powders and aqueous suspensions. *Colloids Surf. A*. 2004. **233**(1–3): 63.
49. Gun'ko V.M. Features of BET method application to various adsorbents. *Him. Fiz. Tehnol. Poverhni.* 2022. **13**(3): 249.
50. Pujari P.K., Sen D., Amarendra G., Abhaya S., Pandey A.K., Dutta D., Mazumder S. Study of pore structure in grafted polymer membranes using slow positron beam and small-angle X-ray scattering techniques. *Nucl. Instrum. Methods Phys. Res., Sect. B.* 2007. **254**(2): 278.
51. Provencher S.W. A constrained regularization method for inverting data represented by linear algebraic or integral equations. *Comput. Phys. Commun.* 1982. **27**(3): 213.
52. Brumberger H. *Small Angle X-ray Scattering*. (New York: Gordon & Breach, 1965).
53. Dieudonné P., Hafidi A.A., Delord P., Phalippou J. Transformation of nanostructure of silica gels during drying. *J. Non-Cryst. Solids.* 2000. **262**(1–3): 155.
54. Fairén-Jiménez D., Carrasco-Marín F., Djurado D., Bley F., Ehrburger-Dolle F., Moreno-Castilla C. Surface area and microporosity of carbon aerogels from gas adsorption and small- and wide-angle X-ray scattering measurements. *J. Phys. Chem. B*. 2006. **110**(17): 8681.
55. Ares A.E. *X-ray Scattering.* (Rijeka, Croatia: InTech, 2017).
56. Gun'ko V.M. Various methods to describe the morphological and textural characteristics of various materials. *Him. Fiz. Tehnol. Poverhni.* 2018. **9**(4): 317.
57. Sternik D., Galaburda M., Bogatyrov V.M., Gun'ko V.M. Influence of the synthesis method on the structural characteristics of novel hybrid adsorbents based on bentonite. *Colloids Interfaces.* 2019. **3**(1): 18.
58. Gun'ko V.M., Meikle S.T., Kozynchenko O.P., Tennison S.R., Ehrburger-Dolle F., Morfin I., Mikhalovsky S.V. Comparative characterization of carbon and polymer adsorbents by SAXS and nitrogen adsorption methods. *J. Phys. Chem. C.* 2011. **115**(21): 10727.
59. Gun'ko V.M. Morphological and textural features of various materials composed of porous or nonporous nanoparticles differently packed in secondary structures. *Appl. Surf. Sci.* 2021. **569**: 151117.
60. Kammler H., Beaucage G., Mueller R., Pratsinis S. Structure of flamemade silica nanoparticles by ultra-small-angle X-ray scattering. *Langmuir.* 2004. **20**(5): 1915.
61. Hyeon-Lee J., Beaucage G., Pratsinis S.E., Vemury S. Fractal analysis of flame-synthesized nanostructured silica and titania powders using small-angle X-ray scattering. *Langmuir.* 1998. **14**(20): 5751.
62. Simmler M., Meier M., Nirschl H. Characterization of fractal structures by spray flame synthesis using X-ray scattering. *Materials*. 2022. **15**(6): 2124.
63. Adamson A.W., Gast A.P. *Physical Chemistry of Surface*. 6th edition. (New York: Wiley, 1997).
64. Gregg S.J., Sing K.S.W. *Adsorption, Surface Area and Porosity*. 2nd ed. (London: Academic Press, 1982).
65. Gun'ko V.M. Textural characteristics of composite adsorbents analyzed with density functional theory and self-consistent regularization procedure. *Him. Fiz. Tehnol. Poverhni.* 2020. **11**(2): 163.
66. Gun'ko V.M. Composite materials: textural characteristics. *Appl. Surf. Sci.* 2014. **307**: 444.
67. McCool B., Murphy L., Tripp C.P. A simple FTIR technique for estimating the surface area of silica powders and films. *J. Colloid Interface Sci.* 2006. **295**(1): 294.

68. Gun'ko V.M., Pakhlov E.M., Skubiszewska-Zięba J., Blitz J.P. Infrared spectroscopy as a tool for textural and structural characterization of individual and complex fumed oxides. *Vib. Spectrosc.* 2017. **88**: 56.
69. Mitchell J., Webber J.B.W., Strange J.H. Nuclear magnetic resonance cryoporometry. *Phys. Rep.* 2008. **461**(1): 1.
70. Strange J.H., Rahman M., Smith E.G. Characterization of porous solids by NMR. *Phys. Rev. Lett*. 1993. **71**(21): 3589.
71. Kimmich R. *NMR Tomography, Diffusometry, Relaxometry*. (Heidelberg: Springer, 1997).
72. Gun'ko V.M. Features of the morphology and texture of silica and carbon adsorbents. *Surface*. 2021. **13(28)**: 127.

*Received 14.06.2022, accepted 03.03.2023*